A THEORITICAL APPROACH TO THE STUDY OF COMPACTION BANDS IN POROUS ROCKS

ARGHYA DAS, GIANG D. NGUYEN, ITAI EINAV

School of Civil Engineering
The University of sydney
Sydney NSW 2006, Australia
email: arghya.das@sydney.edu.au, giang.nguyen@sydney.edu.au, itai.einav@sydney.edu.au,
Web page: http://sydney.edu.au/

Key words: Compaction band, Breakage mechanics, Localization analysis, Grain crushing, Rate dependency, Boundary value problem.

Summary. *The formation and propagation of compaction bands in high porosity sandstones is theoretically investigated in this paper using a new constitutive model based on the recently developed continuum breakage mechanics theory* [1,2]. *This model possesses a micromechanics-based link between the evolving grain size distribution (gsd) and the macroscopic stress strain relationship, through an internal variable called Breakage. This is an advanced feature over many existing plasticity based models in the literature, helping to faithfully track the evolving gsd and its related physics (e.g. permeability reduction). A localization analysis based on the acoustic tensor* [3] *is performed to determine both the onset and orientation of compaction bands due to grain crushing. It is shown that the model used is able to capture well both the material behaviour and formation of compaction band experimentally observed. An enhancement using rate-dependent regularization is applied to the model to deal with instability issues in the analysis of Boundary Value Problems. Based on the regularised model, the formation and propagation of compaction bands due to grain crushing is analysed through a numerical experiment on a porous rock specimen under triaxial loading condition. Good agreement between numerical predictions and experimental observations demonstrates the capability of the new model.*

1 INTRODUCTION

The formation of localization bands in high porosity sandstones involves several micromechanical processes such as grain crushing, grain sliding, bond breaking and pore collapse [4,5]. Shearing at low confining pressures facilitates the fracture of grain bonding cement, allowing the grains to rotate and slip, which could be followed by the flow of granulated material. This bond breaking also reduces the mobilized shear strength, observed through the shear stress drop in experiments. In contrast, shearing at high confining pressures leads to grain crushing followed by pore collapse. During this process, the contacting grains tend to crush under the pressure, leading to the rearrangement of fragments, which further reduces the porosity and consequently hardens the material [4,6]. In this sense, pore collapse acts as a passive mechanism facilitated by a grain-crushing event. At a macroscopic level,

these failure mechanisms can be classified as brittle failure under low pressure and cataclastic flow with shear-enhanced compaction in high-pressure regimes [6]. Although these physical insights on the failure of porous sandstones are well understood, their theoretical modeling is still a challenging task.

Continuum approach based on plasticity theory has been widely used for the prediction of compaction localization in porous rocks [7-12]. In these continuum approaches a bifurcation condition [3], as a material instability condition, is usually employed for the detection of both the onset and orientation of localization bands. It is however unclear whether the parameters giving a good prediction of compaction localization in these models correspond to an experimentally observed response. In other words, the capability of the model to capture the observed material responses is usually left untouched in these studies, while much attention is paid to adjusting model parameters for the prediction of compaction localization. In addition, the underlying evolving microstructures (e.g. grain size distribution) are not fully reflected in those models. It has been showed that these plasticity-based models can lead to erroneous predictions of the permeability changes due to grain crushing [15]. Consequently, despite their good theoretical predictions, lack of a sound physical basis seems to impair the usefulness of these models.

A new continuum model based on the breakage mechanics theory [1,2] has shown its capability in capturing the compaction band formation in porous rocks [13]. The main feature of this theory is that it can take into account the grain crushing effects on the constitutive behavior through an internal variable (called Breakage, B) of the continuum model. This internal variable is explicitly linked with the evolving grain size distribution (gsd), helping to continuously track the gsd during the crushing induced deformation process. The effects of pore collapse on the macroscopic behavior of the material are also accounted in this models based on breakage mechanics theory. A recent study [13] showed that this breakage mechanics model predicts well both the formation and orientation of compaction bands, besides its capability to capture the behavior of porous rocks under high confining pressures [15].

In this paper, the formation and propagation of compaction bands in high porosity sandstones is studied using the above model. An enhancement employing rate dependent regularization is incorporated in this constitutive model to deal with instability issues due to softening and strain localization. Numerical analyses of a porous rock sample under drain triaxial condition are carried out to study the formation and propagation of compaction band. The obtained numerical results are validated against experimental observations.

2   A CONSTITUTIVE MODEL BASED ON BREAKAGE MECHANICS

A brief outline of a model based on breakage mechanics theory is presented in this section. The details of the theory and the development of several constitutive models based on this theory can be found in the papers by Einav [1,2,14] and Nguyen and Einav [15]. Due to grain crushing, the gsd evolves during the deformation of crushable granular materials. In breakage mechanics theory [1,2] this evolution of the current gsd $p(d)$ is directly tracked through an internal variable, called Breakage (B) by the following relationship:

$$p(B,d) = (1-B)p_0(d) + Bp_u(d) \qquad (1)$$

where d is the grain diameter, $p_0(d)$ is the initial *gsd* and $p_u(d)$ is the ultimate *gsd*, which can be conveniently assumed to be of fractal type.

The stress-strain relationship is:

$$\boldsymbol{\sigma} = (1 - \vartheta B)\mathbf{D} : \left(\boldsymbol{\varepsilon} - \boldsymbol{\varepsilon}^p\right) \tag{2}$$

where $\boldsymbol{\sigma}$ is Cauchy stress tensor; $\boldsymbol{\varepsilon}$ and $\boldsymbol{\varepsilon}^p$ are the total and plastic strain tensors respectively; $\mathbf{D}$ is the linear (isotropic) elastic tangent stiffness tensor; the grading index ϑ which is a result of the statistical homogenization, can be obtained from the initial and ultimate *gsd*'s as

$$\vartheta = 1 - J_{2u}/J_{20} \tag{3}$$

where J_{20} and J_{2u} are second order moments of initial and final *gsd* [1]. Einav [14] derived the following elastic-plastic-breakage yield criterion in mixed stress-energy space considering the energy balance driving particle breakage.

$$y = \frac{(1-B)^2 E_B}{E_c} + \left(\frac{q}{Mp}\right)^2 - 1 \leq 0 \tag{4}$$

where E_c is the critical breakage energy which can be determined directly from the isotropic crushing pressure through the relationship $E_C = P_{cr}^2 \vartheta/2K$ [2]; $p = -(1/3)\boldsymbol{\sigma} : \boldsymbol{\delta}$ is the mean stress (positive in compression); $q = \sqrt{(3/2)\mathbf{s} : \mathbf{s}}$ is the distortional stress ($\mathbf{s} = \boldsymbol{\sigma} + p.\boldsymbol{\delta}$ is the deviatoric stress; $\boldsymbol{\delta}$ is Kronecker delta); M is the slope of the critical state line in $p - q$ space; and E_B is the energy thermodynamically conjugated to the breakage internal variable.

$$E_B = \frac{2}{(1-\vartheta B)^2}\left(\frac{p^2}{K} + \frac{q^2}{3G}\right) \tag{5}$$

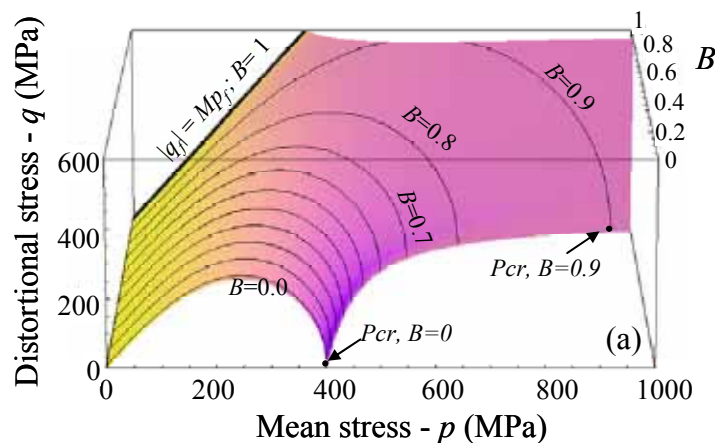A typical evolving yield envelope in *p-q-B* space is plotted in Fig. 1.

Figure 1: Typical yield surface in *q-p-B* space

The evolution rules for breakage and plastic strain are respectively,

$$dB = 2d\lambda (1-B)^2 \cos^2\omega \big/ E_c \text{ and} \tag{6}$$

$$d\boldsymbol{\varepsilon}^p = d\lambda \left(-2\frac{(1-B)^2 E_B \sin^2\omega}{pE_c}\frac{\boldsymbol{\delta}}{3} + \frac{3\mathbf{s}}{M^2 p^2} \right). \tag{7}$$

In the above expression, ω is the parameter that couples the plastic volumetric deformation with grain crushing [2]. Physically, ω represents the pore collapse of the material, which is a consequence of grain crushing and grain/fragment reorganization. Further details on ω and pore collapse can be found in Einav [1, 2] and Das et al. [13].

3 ANALYSIS OF COMPACTION LOCALIZATION

3.1 Model behavior

The model behavior is presented in this section. The model parameters for a typical high porosity (23%) sandstone, the *Bentheim* sandstone are determined from experimental data. In particular, the stiffness (G, K), critical state parameter (M) and critical breakage energy (E_c) are obtained from published experimental stress-strain responses [16,17]. The grading index ϑ is determined from basic *gsd* [18] information and the assumption of power law distribution for both initial and final *gsd*. The coupling angle (ω) is chosen by matching the inelastic stress-strain response with experimental results. Details on the model calibration can be found in Das et al. [13] and corresponding model parameters are listed in table 1.

Table 1: Model parameters

Parameters	Value
G	7588 MPa
K	13833 MPa
M	1.7
E_c	4.67 MPa
ϑ	0.85
ω	70°

Fig. 2 presents the model behavior based on the model parameters in Table 1. The predicted stress-strain responses are found to be in good agreement with experimental observations.
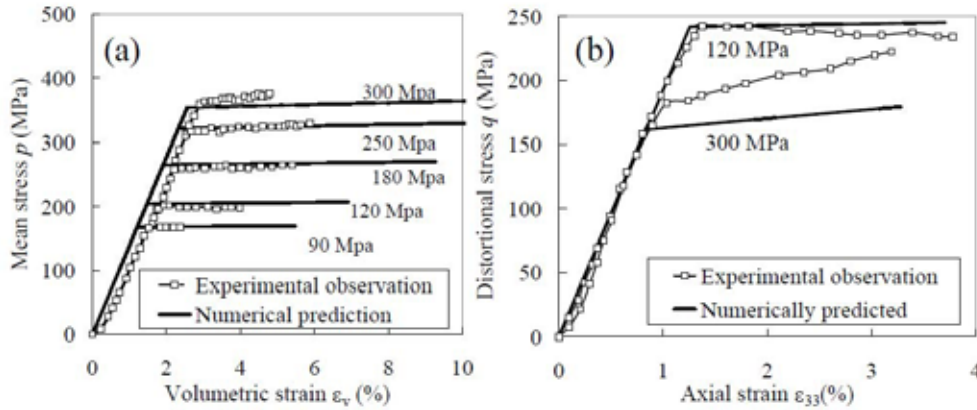
Figure 2: Numerical and experimental [19] comparisons of stress-strain responses of Bentheim sandstone under drained triaxial loading at different confining pressures; (a) mean stress vs. volumetric strain; (b) differential stress vs. axial strain.

3.2 Numerical prediction of compaction localization

We use the discontinuous bifurcation condition described in Rudnicki and Rice [3] to detect the formation of compaction band. Eq. 8 represents the simplified form of discontinuous bifurcation condition, considering the fact that the tangent stiffnesses of the material inside and outside the band are different in the case of breakage model [3,20].

$$\left| \mathbf{n} \cdot \mathbf{L}^i \cdot \mathbf{n} \right| = \left| \mathbf{A} \right| \le 0 . \tag{8}$$

In the above equation $\mathbf{n}$ is the band orientation vector; $\mathbf{L}^i$ is the tangent stiffness tensor inside the localization zone (eq. 9); $\mathbf{A}$ is the strain localization tensor, also termed the acoustic tensor. The following tangent stiffness tensor is obtained using the model described in section 2. The details on the formulation of this forth order stiffness tensor were already given in Das et al. [13].

$$\mathbf{L}^i = \left(1 - \vartheta B \right) \mathbf{D} - \frac{\left(1 - \vartheta B \right) \left[\left(1 - \vartheta B \right) \mathbf{D} : \frac{d\boldsymbol{\varepsilon}^p}{dB} + \frac{\vartheta \boldsymbol{\sigma}}{\left(1 - \vartheta B \right)} \right] \otimes \left[\mathbf{D} : \left(\frac{\partial y}{\partial p} \frac{\partial p}{\partial \boldsymbol{\sigma}} + \frac{\partial y}{\partial q} \frac{\partial q}{\partial \boldsymbol{\sigma}} \right) \right]}{\left(\frac{\partial y}{\partial p} \frac{\partial p}{\partial \boldsymbol{\sigma}} + \frac{\partial y}{\partial q} \frac{\partial q}{\partial \boldsymbol{\sigma}} \right) : \left[\left(1 - \vartheta B \right) \mathbf{D} : \frac{d\boldsymbol{\varepsilon}^p}{dB} + \frac{\vartheta \boldsymbol{\sigma}}{\left(1 - \vartheta B \right)} \right] - \frac{\partial y}{\partial B}} \tag{9}$$

We show that the model described in the previous sections is capable of capturing the experimentally observed localization features of porous rocks, besides its capability in describing the material behavior (section 3.1). Fig. 3a highlights (the thick black line) the set of favorable stress states for the formation of localization band at the onset of yielding. The results are compared with their experimental counterpart [19]. At much higher-pressure regime, no localization failure is observed at the onset of inelastic deformation. As also numerically experienced, the closer to the isotropic compression line the stress path is, the easier the deformation would evolve into cataclastic flow without any compaction localization. However, shearing beyond elastic limit also eventually induces compaction
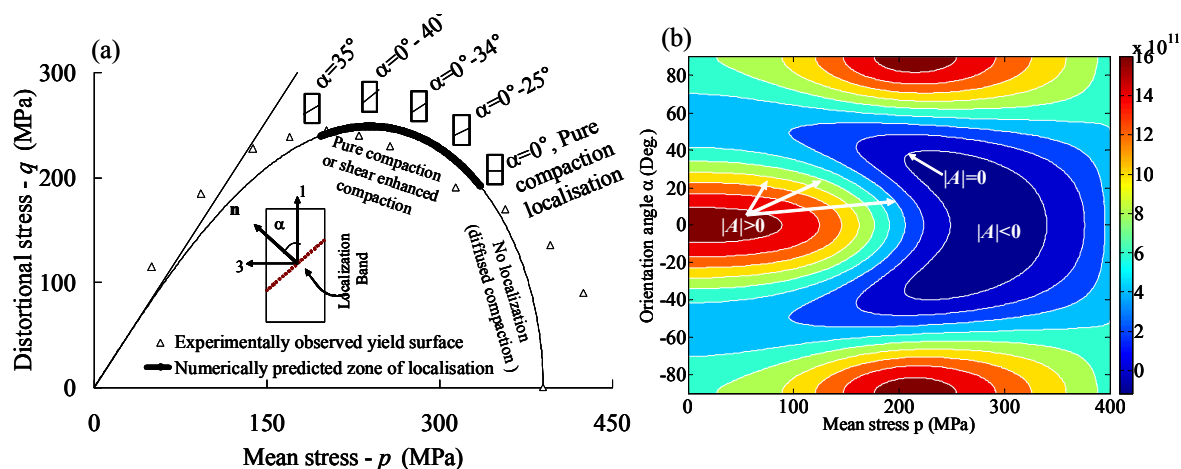
localization.

Figure 3: (a) Initial yield envelope and predicted stress states at the formation of compaction localization for Bentheim sandstone. (b) Corresponding contour of determinant of the acoustic tensor.

Fig. 3b shows the contours of the determinants of the acoustic tensor against the band orientation angle (α) and the mean stress (p). In this figure the inner most zone, where the determinant of the acoustic tensor is negative ($|\mathbf{A}| < 0$), indicates localization failure. It can be seen from Eq. 8 and Fig. 3b that for a given confining pressure p, there is a set of possible orientation angles for the localization band. From the experimental point of view, localization bands having orientation angle $0° \leq \alpha \leq 10°$ can be classified as pure compaction band whereas those with $10° \leq \alpha \leq 45°$ are treated as shear enhanced compaction bands [19]. Our analysis predicts that the band orientation for a wide range of confining pressure falls within the range of $0°$ to $40°$ that is close to the experimental observations in [19].

4 RATE DEPENDENT REGULARIZATION

4.1 Perzyna type rate dependent regularization

Due to the localization characteristics of the model, the boundary value problems (BVP) become ill-posed and hence treatment for this instability is needed. Introduction of material rate dependency, which implicitly introduces a length scale in to the governing constitutive equation [21], is one of the ways to make the BVPs well-posed. Here we incorporate rate effect in the breakage constitutive model presented in the preceding section using Perzyna type overstressed function. The model enhancement is carried out by modifying the evolution laws of breakage and plastic strain in the following manner.

$$\mathrm{d}B = \frac{\langle y^N \rangle}{\eta} \frac{2(1-B)^2 \cos^2\omega}{E_c} \mathrm{d}t \text{, and} \tag{10}$$

$$\mathrm{d}\boldsymbol{\varepsilon}^{vp} = \frac{\left\langle y^N \right\rangle}{\eta}\left(-2\frac{(1-B)^2 E_B \sin^2 \omega}{pE_c}\frac{\boldsymbol{\delta}}{3} + \frac{3\mathbf{s}}{M^2 p^2} \right)\mathrm{d}t \,. \tag{11}$$

It is noted that the viscosity parameter η is a dimensional quantity ($M^{-1}LT^3$) when used with this breakage model. Comparing the rate dependent flow condition with conventional rate independent evolution law, we can express the non-negative multiplier or consistency parameter as,

$$\mathrm{d}\lambda = \frac{\left\langle y^N \right\rangle}{\eta}\mathrm{d}t \,. \tag{12}$$

As can be seen, the Perzyna-type rate dependent breakage model provides an explicit form for the non-negative multiplier.

4.2 Rate effect on constitutive response
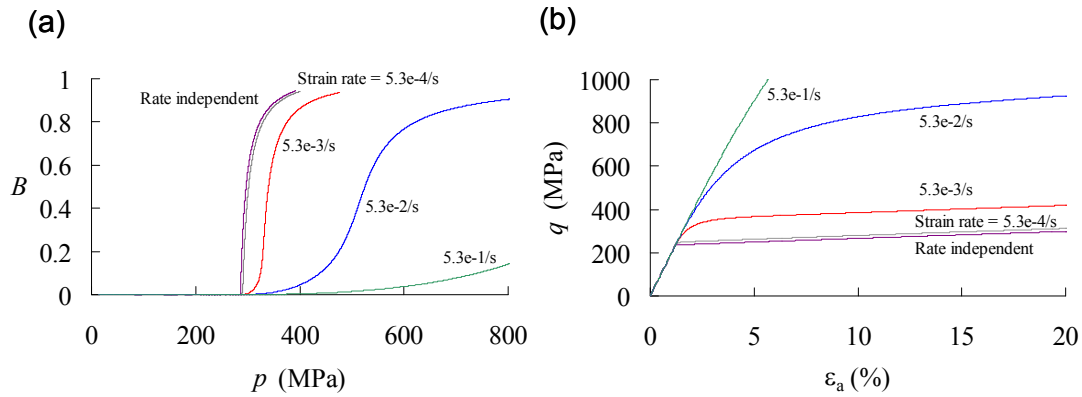
(a)　　　　　　　　　　　　　　　(b)

Figure 4: Effect of strain rate on the model response in drained triaxial loading - (a) breakage against mean stress; (b) distortional stress against axial strain.

　　Numerical drained triaxial tests are carried out to observe the effect of increasing strain rate on the material behavior. The same model parameters listed in Table 1 are used. Other parameters related to the rate dependency are, $N = 1.0$; and viscosity parameter $\eta = 1.0$ sec/kPa. In the numerical tests, the strain rate is increased via controlling the time increment (e.g. $\mathrm{d}t = 1s, 0.1s, 0.001s,$ and $0.0001s$, corresponding to the strain rates indicated in Fig. 4). Fig. 4b indicates that with increasing strain rates the ultimate stress is also increasing. The transition from elastic to inelastic zone is smoother with increasing strain rate. On the other hand, at slow strain rates the model response approaches rate independent behavior. Besides the stress-strain response, the rate of breakage growth reduces with the increase in strain (Fig. 4a). From the microscopic point of view, high strain rate does not allow sufficient time to break or rearrange the grains [22]. Thus, the material becomes stronger and this feature is also reflected in the macroscopic stress-strain response of the proposed model.

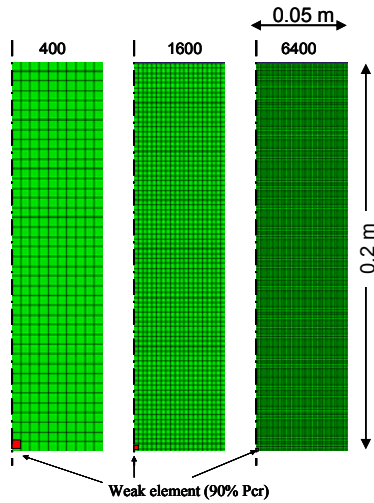## 4.3 Mesh independency of finite element solutions

Figure 5: FE meshing for triaxial drained test

The stability of the above rate dependent breakage constitutive model is illustrated through the numerical analysis of a rock specimen under drained triaxial loading condition. The commercial package Abaqus (version - 6.8) is used for the entire finite element analysis. We construct the model (0.1 x 0.2 m) using linear quadrilateral finite elements (Fig. 4). Due to symmetry in geometry and loading, only half of specimen is modelled. The analysis is performed considering axisymmetric 2D plane strain condition with strain controlled loading. The entire loading arrangement is a two stage process where initially we apply a confining pressure and allow the material to deform isotropically. Thereafter axial load, through prescribed vertical displacement producing a constant axial strain rate of $5.3*10^{-4}$/s, is applied to the specimen, while the confining stress is kept constant. The boundary conditions are: restricted vertical movement of the bottom boundary; and (fixed) incremental vertical displacement at the top boundary. To trigger off the localization we introduce local anisotropy via a weak element having lower crushing pressure (90% of P_{cr}) (Fig. 5).
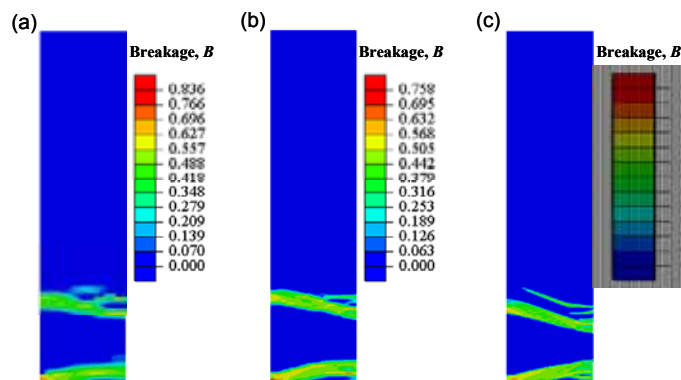

Figure 6: Breakage contours showing the formation of shear enhanced compaction band under drained triaxial test at 3% axial strain (a) 400 elements; (b) 1600 elements; (c) 6400 elements.

The effect of the spatial discretization on the numerical solutions is presented in Fig. 5. We use three different finite element meshes employing 400 elements, 1600 elements and 6400 elements, respectively. The contours in Fig. 5 indicate the growth of breakage during the deformation of the specimen. As can be seen, the localization zones and their widths are almost identical for all three cases of discretization The regularization effect of the rate dependent enhancement is clearly visible from the global load-deflection curves (Fig. 7), in which the trends of the curves and their periods of oscillation are almost identical.
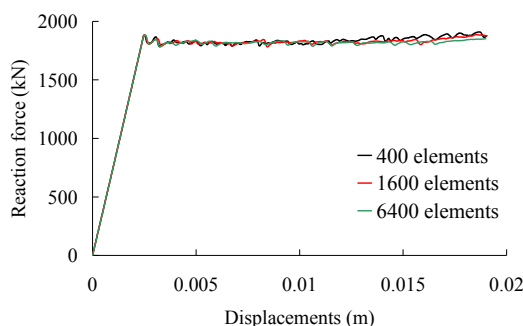

Figure 7: Reaction force against displacement plot for drained triaxial test

5 COMPACTION BAND PROPAGATION IN POROUS ROCKS

It is clear from the previous analysis that the use of rate effect eliminates the pathological mesh sensitivity of the numerical solutions. The propagation of compaction bands is studied in this section using the FE mesh consists of 1600 elements. We start the numerical drained shear test with an initial isotropic pressure of 300 MPa. The same axial strain rate of $5.3*10^{-4}$ /s, as used in section 4.3, is applied to the top of the specimen in the second stage of loading.
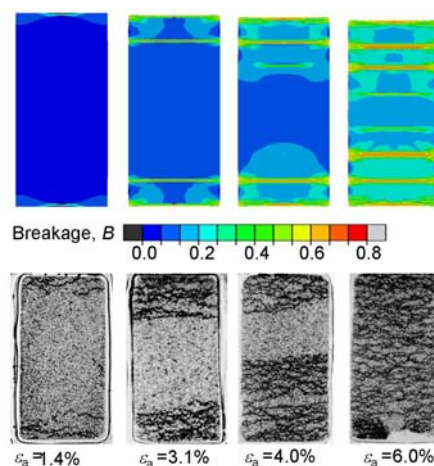

Figure 8: Breakage contours showing pure compaction band formation in drained triaxial test at different axial strains, (a) Numerical simulation; (b) Experimental observation [19].

From laboratory experiments it has been observed and reported [23,24] that compaction band initiates from the two ends of the sample due to the stiffness mismatch between the material

and the cap of testing device. To simulate similar band initiation we introduce two weaker finite elements at both ends of the numerical sample.

The breakage contours in Fig. 8 show the propagation of compaction bands during the shearing process. The colour code indicates intense grain crushing via breakage growth that takes place inside the compaction bands. As expected, compaction localization occurs at the two ends of the specimen and propagates towards its centre (Fig. 8). Baud et al. [19] also reported similar band propagation in their experimental results. This is manifested because of simultanous loading and unloading process during shearing at high confining pressure.
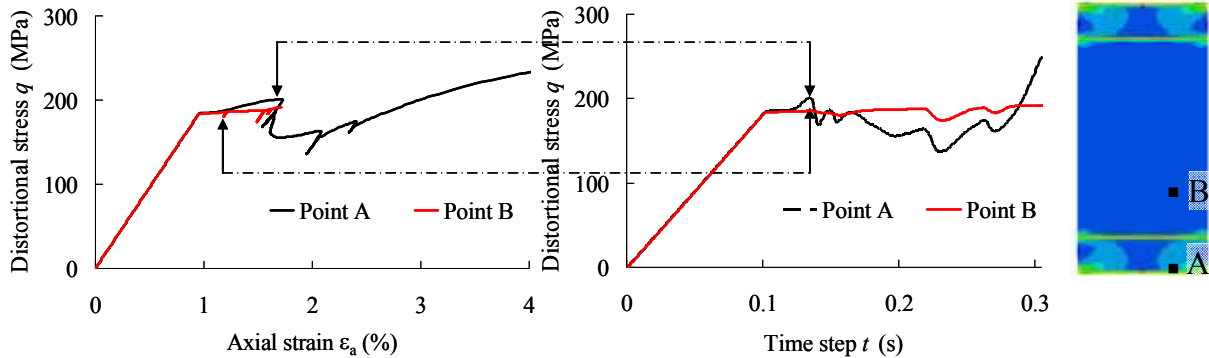

Figure 9: Stress responses at integration points (A and B) of numerical sample, (a) against axial strain; (b) against time, for a fixed time span.

The variation of distortional stress against time and axial strain is plotted in Fig. 9a,b for two integration points *A* and *B*. Due to the confinement and the varying inhomogeneous state (of stress, strains and breakage), the behavior of material points along the specimen height switches among hardening, softening, and elastic unloading. These material points take turn in the crushing process. Due to this process of simultaneous loading and unloading, compaction bands propagate from the two ends of the sample towards its centre, at discrete locations along the specimen height. This effect is also visible through the oscillating nature of the global stress strain response during shearing (Fig. 10).
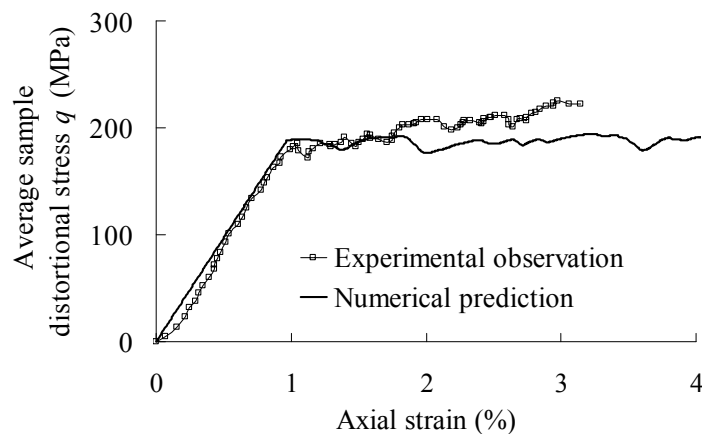

Figure 10 Global stress-strain response from numerical prediction and experimental observation [19]

The predicted average distortional stress-strain response and experimental observations [19] are plotted in Fig.10. These macroscopic model responses can be seen to be in good agreement with its experimental counterpart.

6 CONCLUSIONS

We show in this study a micromechanics-based constitutive model capable of capturing both the material behavior and the formation of compaction bands. The enhancement of this model to deal with material instability issues, using rate dependent regularization, allows us to to numerically explore the propagation of compaction bands in a porous rock specimen. The obtained numerical results are in good agreement with experimental observations, thus demonstrating the capability of the proposed model. This is an important starting point for a deeper study on the initiation and propagation of compaction bands in porous rocks.

REFERENCES

[1] Einav, I., Breakage mechanics—Part I: theory. *Journal of the Mechanics and Physics of Solids* (2007) **55**:1274-1297.

[2] Einav, I., Breakage mechanics—Part II: modelling granular materials. *Journal of the Mechanics and Physics of Solids* (2007) **55**:1298-1320.

[3] Rudnicki, J.W. and Rice, J.R., Conditions for the localization of deformation in pressure-sensitive dilatant materials. *Journal of the Mechanics and Physics of Solids* (1975) **23**:371-394.

[4] Menéndez, B., Zhu, W., and Wong, T.-f, Micromechanics of brittle faulting and cataclastic flow in berea sandstone. *Journal of Structural Geology* (1996) **18**:1-16.

[5] Wu, X.Y., Baud, P., and Wong, T.-f, Micromechanics of compressive failure and spatial evolution of anisotropic damage in darley dale sandstone. *International Journal of Rock Mechanics and Mining Sciences* (2000) **37**:143-160.

[6] Wong, T.-f, David, C., and Zhu, W., The transition from brittle faulting to cataclasic flow in porous sandstones:mechanical deformation. *Journal of Geophysical Research* (1997) **102**:3009-3025.

[7] Olsson, W.A., Theoretical and experimental investigation of compaction bands in porous rock. *Journal of Geophysical Research* (1999) **104**:7219-7228.

[8] Issen, K.A. and Rudnicki, J.W., Conditions for compaction bands in porous rock. *Journal of Geophysical Research* (2000) **105**:21529-21536.

[9] Rudnicki, J.W., Shear and compaction band formation on an elliptic yield cap. *Journal of Geophysical Research* (2004) **109**:1-10.

[10] Challa, V. and Issen, K.A., Conditions for compaction band formation in porous rock using a two-yield surface model. *Journal of Engineering Mechanics* (2004) **130**:1089-1097.

[11] Chemenda, A.I., The formation of tabular compaction-band arrays: theoretical and numerical analysis. *Journal of the Mechanics and Physics of Solids* (2009) **57**:851–868.

[12] Sternlof, K.R., Rudnicki, J.W., and Pollard, D.D., Anticrack inclusion model for compaction bands in sandstone. *Journal of Geophysical Research* (2005) **110**:1-16.

[13] Das, A., Nguyen, G.D., and Einav, I., Compaction bands due to grain crushing in porous rocks : a theoretical approach based on breakage mechanics. *Journal of Geophysical Research* (2011):(accepted in press).

[14] Einav, I., Soil mechanics: breaking ground. *Philosophical transactions. Series A, Mathematical, physical, and engineering sciences* (2007) **365**:2985-3002.

[15] Nguyen, G.D. and Einav, I., The energetics of cataclasis based on breakage mechanics. *Pure and Applied Geophysics* (2009) **166**:1693–1724.

[16] Wong, T.-f, Baud, P., and Klein, E., Localized failure modes in a compactant porous rock. *Geophysical Research Letters* (2001) **28**:2521-2524.

[17] Baud, P., Vajdova, V., and Wong, T.-f, Shear-enhanced compaction and strain localization: inelastic deformation and constitutive modeling of four porous sandstones. *Journal of Geophysical Research* (2006) **111**:1-17.

[18] Schutjens, P.M.T.M., Hausenblas, M., Dijkshoorn, M., and Munster, J.G.V., The influenec of intergranular microcracks on the petrophysical properties of sandstone - experiments to quantify effects of core damage. , *International Society of the Society of Core Analysts*, 1995, :1-12.

[19] Baud, P., Klein, E., and Wong, T.-f, Compaction localization in porous sandstones: spatial evolution of damage and acoustic emission activity. *Journal of Structural Geology* (2004) **26**:603-624.

[20] Chambon, R., Crochepeyre, S., and Desrues, J., Localization criteria for non-linear constitutive equations of geomaterials. *Mechanics of Cohesive-frictional Materials* (2000) **5**:61-82.

[21] Needleman, A., Material rate dependence and mesh sensitivity in localization problems. *Computer Methods in Applied Mechanics and Engineering* (1988) **67**:69-85.

[22] Yamamuro, J.A. and Lade, P.V., Effects of strain rate on instability of granular soils. *Geotechnical Testing Journal* (1993) **16**:304.

[23] Olsson, W.A., Quasistatic propagation of compaction fronts in porous rock. *Mechanics of Materials* (2001) **33**:659-668.

[24] Katsman, R., Aharonov, E., and Scher, H., Numerical simulation of compaction bands in high-porosity sedimentary rock. *Mechanics of Materials* (2005) **37**:143-162.